Special Issue: AFOSR

JOURNAL OF COMPOSITE MATERIALS

Journal of Composite Materials
2022, Vol. 0(0) 1–11

DOI: 10.1177/00219983221146618
journals.sagepub.com/home/jcm
SAGE

Liquid crystal elastomer composite-based photo-oscillator for microrobots

Pengju Shi, Yusen Zhao, Zixiao Liu and Ximin He

Abstract

In recent years, photoactive materials have attracted extensive interest in microrobots for their attractive abilities of untethered and tunable control with light. Conventional photo-oscillators based on Azo-containing liquid crystal network require complex surface alignment techniques and light sources with specific wavelengths and polarity, which limits their application in controlled autonomy. Here, we report a facile strategy to create self-oscillating microrobots powered and controlled by a wide spectrum of constant light. The oscillators are composed of a layer of candle soot (CS)-containing liquid crystal elastomer (LCE) attached to a layer of polydimethylsiloxane (PDMS). The strip-shaped oscillators with one end fixed can execute self-sustained oscillation through a self-shadowing mechanism. LCEs with CS as an excellent photo-absorber provides superior photothermal actuation, while PDMS with low viscoelasticity accelerates the actuation-recovery cycle of the oscillator. Our LCE composite photo-oscillators show tunable frequencies and amplitudes by structural and light intensity modulation, showing potential for autonomous soft robotic applications.

Keywords

liquid crystal elastomer, candle soot, photothermal actuation, self-oscillation

Introduction

Stimuli-responsive soft materials have attracted extensive interest in the field of soft robotics and smart systems, because they mimic living organisms' ability to respond and adapt to environmental cues to perform different modes of motion and execute various functions on demand without human intervention.[1–3] Among them, liquid crystal polymers (LCPs),[4–6] shape-memory polymers,[7–9] and hydrogels[10–12] can respond to multiple stimuli including heat,[13–15] light,[16–19] electric current,[19,20] magnetic field,[21,22] and chemical stimuli[15,23,24] by doping the pure materials with fillers or copolymerizing with functional moieties. Compared to other forms of stimuli, light is a clean and ubiquitous stimulus that offers remote and localized control, and multiple tunability (wavelength, intensity, and polarity).[25–27]

Liquid crystal polymer emerges as a powerful candidate for photo-driven soft robots due to its rapid response to stimuli, and reversible anisotropic deformation induced by liquid crystal (LC) phase transition.[28–31] Specifically, when a monodomain LCP transits from an LC phase to an isotropic phase, it will contract along the long axis of mesogen (director) and expand along the short axis. Two mechanisms have been adopted to endow photo-responsiveness to LCP. In a photochemical route, the LCP contains copolymerizable photoswitches like azobenzene-derivative mesogen that undergoes cis-trans isomerization under UV and visible irradiation, leading to the disruption and restorage of LC order. For example, Serak et al. reported an oscillating liquid crystal network (LCN, heavily crosslinked LCP) cantilever film exposed to Ar^+ laser.[32] In a photothermal route, a photothermal dye can be copolymerized into LCN to transform light to heat that is imparted to the polymer matrix, so that the LCN is heated over the nematic-to-isotropic phase transition temperature (T_{NI}). Gelebart et al. reported a locomotive LCN robot performing wave propagation with snap-through instability.[17] However, LCN can suffer from the following issues that restrict their further application in real life: (1). Complex surface alignment technique is required to yield mesogen alignment in LCN, so that LC phase transition can trigger bending of the LCN film; (2). Specific light sources are required as co-polymerized photoswitches or photothermal agents respond

Department of Material Science and Engineering, University of California Los Angeles, Los Angeles, CA USA

Corresponding author:
Ximin He, Department of Materials Science and Engineering, University of California Los Angeles, 410 Westwood Plaza, Eng-V, Los Angeles, CA 90095, USA.
Email: ximinhe@ucla.edu

to light of specific wavelengths and polarization; (3). Functionality can only be introduced through copolymerization, limiting the chemistry available to modify the polymer, while dopants usually cannot disperse well in the heavily crosslinked polymer matrix.[17,18,33]

Liquid crystal elastomer (LCE) with a loosely crosslinked network has potential to circumvent the aforementioned issues. Uniaxial mechanical stretching can be used to fabricate planar aligned LCE facilely with large scales.[34] To render photoresponsive properties to LCE matrix, photothermal agents can be designed and incorporated into LCE to enable broad-spectrum absorption.[30] Conventional photothermal agents including carbon-based nanomaterials, metallic nanomaterials, and dyes can be doped into LCE.[4,33,35] However, they usually have the disadvantage of complicated synthesis, poor compatibility with LCE matrix, high price, and/or negative environmental impact, which limits the application of these photothermal agents in broader context.[30] Furthermore, there have been many reports of photo-driven LCE doped with photothermal agents realized multiple modes of motion including walking, crawling, rolling, and jumping.[13,36,37] However, to the best of our knowledge, it remains challenging to achieve autonomous oscillatory motion in LCE monolith, because its planar configuration and fast thermal diffusion throughout thickness will lead to linear contraction rather than angular bending.

In recent years, candle soot (CS) has been discovered as a photothermal agent with superior photothermal conversion efficiency and applied in realms of anti-icing and solar vapor generation applications.[38,39] The transition of CS from an industrial waste to a functional material is in line with the principle of green chemistry.[40] Nevertheless, there has been no attempt to utilize it as a photothermal agent to fuel a photo-driven actuator. CS is produced from incomplete combustion of wax and mainly composed of carbon nanoparticles, hydrocarbons, and carboxylic acids.[40] The polar functional groups in CS enable it to disperse thoroughly in polar solvents like alcohols, chloroform, and acetone.[41,42] Inspired by this feature, we also discovered that CS disperse well in polymer matrix, making it an ideal photothermal agent for LCE actuation.

To overcomes the aforesaid issues, herein we propose a facile fabrication of a bilayered LCE-CS/PDMS composite for making photo-oscillators with tunable self-sustained oscillatory behaviors under wide-spectrum light (Figure 1(a) and (b)). The LCE is fabricated via a 2-step thiol-acrylate Michael addition polymerization, with RM257 as mesogen, 1.6-hexanedithiol (HDT) as the chain extender, and pentaerythritol tetrakis (3-mercaptopropionate) (PETMP) as the crosslinker (Figure 1(c)). CS is doped into the LCE matrix as the photothermal agent to provide photothermal responsiveness. A layer of temperature-insensitive polydimethylsiloxane (PDMS) is attached conformably to the LCE-CS film (Figure 1(b)), to create a bimorph material and facilitate the bending upon illumination on the LCE-CS film. Specifically, when LCE-CS is heated upon exposure to irradiation, the LCE-CS layer will contract, while PDMS layer remains approximately the same length. As result, there will be a bending motion towards the LCE-CS side. Under irradiation of a spot light source on the LCE-CS side of the bilayer, self-oscillation is achieved with a self-shadowing mechanism (Figure 1(d)). The irradiation spot will be heated up and serve as a hinge, around which the bilayer bends and rotates, lifting the tip of the bilayer. As a result, the light path will be blocked by the tip, allowing the hinge to cool down and recover, which in turn exposes the hinge to irradiation again. A self-regulating negative feedback loop of temperature and motion is thus created. Such a LCE-CS/PDMS bilayer has presented a great oscillation performance, which may be attributed to the following reasons: (1). CS has a higher photothermal conversion efficiency and better compatibility with LCE than traditional photothermal agents like carbon nanotubes (CNT). (2). PDMS as a passive layer with low viscoelasticity provides a recovery force that accelerates the actuation-recovery cycle. In addition, we show that the oscillation frequency and amplitude are tunable by simply tailoring the geometry of the photo-oscillator (length, thickness ratio, etc.) and the intensity of light.

Experimental

Materials and specimen preparation

Preparation of candle soot. An aluminum foil was held 1 cm above an ignited paraffin candle (Hyoola, white pillar candles, unscented) so that it was in contact with the inner flame to collect the CS. Then, CS was scraped off from the aluminum foil using a razor blade and collected in a glass vial without further treatment.

Preparation of mold. Glass slides were cut into dimensions of 50 × 40 mm and cleaned by sonication (Branson 5800) in ethanol for 15 min. The cleaned glass slides were blown dry under a flow of air. Paper tapes were cut into strips of 40 × 3 mm, and 2 layers of tape (VWR 89087-960, 0.2 mm thick in total) were taped onto both ends of the glass slides as spacers. After casting of the reaction mixture (see Preparation of LCE-CS composite) onto a glass slide with spacers (substrate), another glass slide (without spacer) was placed on top of the substrate to form a cell. Both ends of the cell were clamped firmly with binder clips.

Preparation of LCE-CS and LCE-CNT composites. 2-Methyl-1,4-phenylene bis(4-(3-(acryloyloxy)propoxy)benzoate) (RM 257) was purchased from Shijiazhuang Sdyano Fine

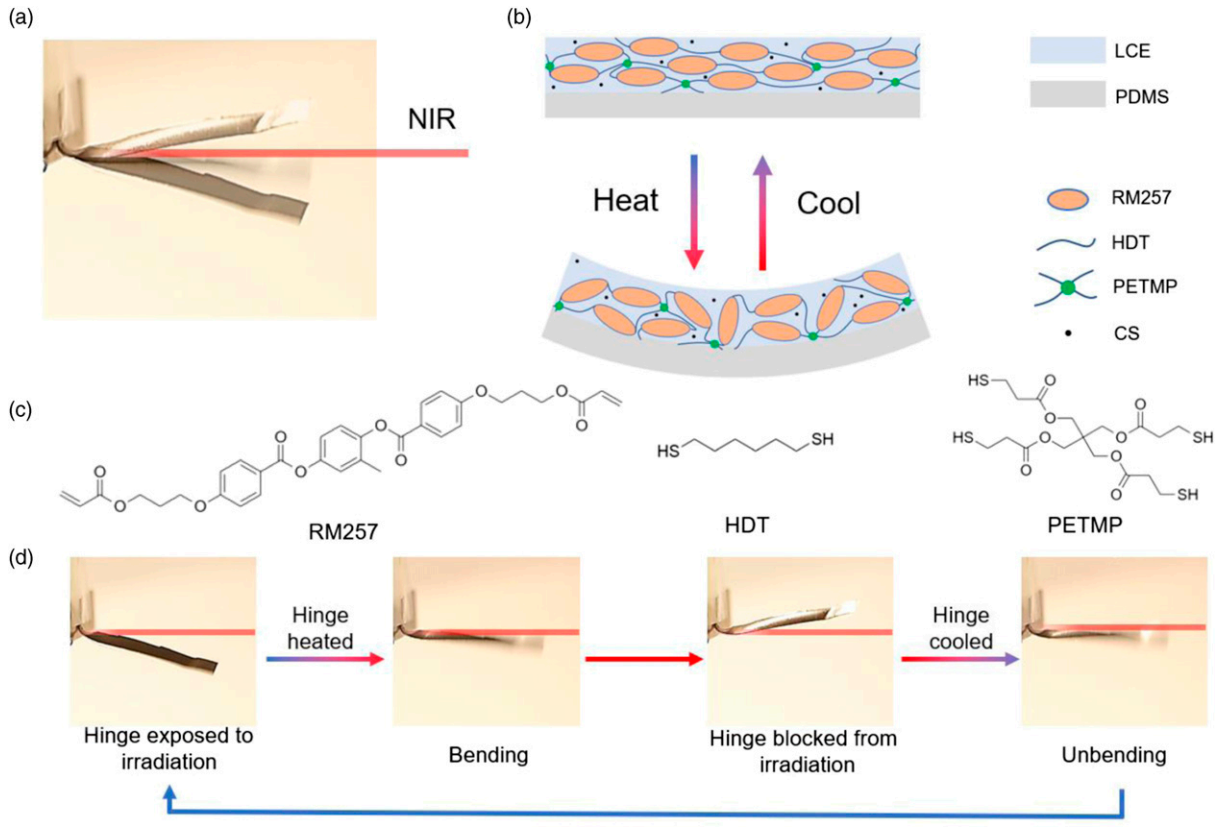

Figure 1. Design and mechanism of LCE-CS/PDMS photo-oscillator (a) Image of photo-oscillator under 808 nm irradiation (superimposed images of multiple snapshots during the oscillation). Red beam shows direction of IR irradiation. (b) Schematic diagram of the LCE-CS/PDMS bilayer. The LCE-CS layer contracts when heated and restores its original shape when cooled, causing the bending and unbending of the bilayer. (c) Structure of chemicals used to synthesize the LCE. (d) The feedback loop created by self-shadowing mechanism. Red beam shows direction of IR irradiation.

Chemical, Co., Ltd. 1.6-hexanedithiol (HDT), 2-hydroxy-4'-(2-hydroxyethoxy)-2-methylpropiophenone (Irgacure 2959), pentaerythritol tetrakis (3-mercaptopropionate) (PETMP), dipropylamine (DPA) and toluene were purchased from Sigma-Aldrich. Polydimethylsiloxane (PDMS) (Sylgard 184) was purchased from Dow Inc. Silicone adhesive was purchased from Loctite. CNT (carbon nanotube multiwalled C2156) was purchased from TCI. All materials were used without further purification.

The LCE was synthesized via a two-step thiol-acrylate Michael addition reaction. Briefly, RM257 and 0.6 wt% of Irgacure 2959 were dissolved by adding 30 wt% of toluene at 80°C. HDT and PETMP were added to the solution, so that 13 mol% of the thiol groups were from PETMP, and the number of acrylate groups was in 2.5% excess of thiol groups. 0.1, 0.25, 0.5, or 1.0 wt% of CS was added to the reaction mixture based on weight of all reactants, excluding the solvent. LCE-CNT composites were prepared in the same way by replacing CS with CNT of the same weight. The reaction mixture was heated to 80°C while vigorously stirred with a magnetic stirrer at 500 r/min. Then the mixture was sonicated using a bath sonicator (Branson 5800) for 20 min.1 mol% of DPA (based on thiol groups) was dissolved in toluene to make a 2 wt% solution. The DPA solution was added dropwise to the reaction mixture with constant stirring. The mixture was cast into a homemade mold as described above. After 24 h of reaction at room temperature, a partially crosslinked film was formed. The film was released from the mold and placed in oven at 55°C for 24 h to remove the solvent. The film was cut into a dog-bone shape using laser cutting and mechanically stretched to 60% strain. Lastly, the stretched samples were fully crosslinked under 365 nm UV irradiation for 30 min.

Preparation of CS/ethylene glycol and CNT/ethylene glycol solutions. 1 mg of CS or CNT were weighed and dispersed into 50 mL of ethylene glycol after sonication (Branson 5800) for 20 min.

Photo-oscillator assembly. Clean glass slides were prepared by sonication (Branson 5800) in water and ethanol for 20 min, respectively, followed by drying under an air flow.

The glass slides were then treated with oxygen plasma to remove any organic residuals. To prepare the PDMS films, Sylgard 184 base and mixture were mixed (base: curer = 5: 1 in weight) and degassed for 30 min under vacuum. The mixture was spin-coated onto the clean glass slides and then cured on a hot plate at 100°C for 2 h. The spinning time was fixed at 2 min and rotation speeds of 180, 360, 720, 1080 r/min were chosen to produce PDMS films with thicknesses of 250, 75, 50, and 32 μm. The PDMS films deposited on the glass slides were soaked in a 10 wt% solution of silicone adhesive in hexanes for 30 s. The LCE samples were pressed firmly onto the PDMS films and allowed to cure for 48 h. The LCE/PDMS bilayers were peeled from the glass slides with a razor blade and then cut into desired shape.

Characterizations of materials

Optical properties and photothermal conversion efficiency of photothermal agents and LCE-CS composite. CS and CNT (for comparison) were dispersed in ethylene glycol at a concentration of 20 μg/mL. The absorption spectra of the solutions from 250 to 1100 nm were measured at room temperature using a UV-Vis-NIR spectrophotometer with corresponding light source (Ocean Optics, USB2000+UV-VIS-ES and DH-2000-BAL). The absorption spectra of LCE-CS and LCE-CNT composites from 300 to 1100 nm were measured using a spectrophotometer (Shimazu, UV-3101PC). Photothermal conversion efficiency of LCE-CS and LCE-CNT composites was measured with a thermal imager (FLUKE, TiX580). The samples were clamped at both ends and exposed to an 808 nm IR light source (Q-BAIHE, LSR808NL) with the intensity varying from 100 to 3000 mW/cm^2. The temperature change at the irradiation position was recorded over time. The light intensity is confirmed using a power sensor (Thorlabs, PM16).

In order to accurately determine the photothermal response of LCE, a theoretical model has been developed to calculate the photothermal conversion efficiency. Based on the energy balance principle,[43] the time variation of temperature T can be derived as

$$\frac{dT}{dt} = \frac{E_{abs} - E_{loss}}{\sum_i m_i C_i} = \frac{P\left(1 - 10^{-A_\lambda}\right)\eta}{\sum_i m_i C_i} - \frac{hS[T(t) - T_0]}{\sum_i m_i C_i} = A - B[T(t) - T_0] \tag{1}$$

where m_i and C_i are the mass and heat capacity of each component in the material system. Since the mass and heat capacity of photothermal agents are negligible compared to the mass and heat capacity of the LCE, assume $i = 1$, and literature value was used for the heat capacity of LCE (C_{LCE} = 0.470 J·°C^{-1}g^{-1}).[44] E_{abs} and E_{loss} are energy absorption and loss, respectively. P is the power of the incident laser, A_λ is the absorbance of the material at the laser wavelength, η is the photothermal conversion efficiency, h is the heat transfer coefficient, S is the area exposed to irradiation, and T_0 is the room temperature. A and B are the parameters related to energy absorption and dissipation, respectively, which need to be further determined by experimental results of temperature variation with time t. Equation (1) can be rearranged and integrated from 0 to t to obtain

$$T(t) = T_0 + \frac{A}{B}\left(1 - e^{-Bt}\right) + (T_{ini} - T_0)e^{-Bt} \tag{2}$$

where T_{ini} is the initial temperature. During heating, $A \neq 0$, $T_{ini} = T_0$, and equation (2) can be written as $T_h(t) = T_0 + (A/B)(1\text{-}e^{-Bt})$. When the material is cooled, $A = 0$, $T_{ini} = T_{max}$, and the temperature variation is captured by $T_c(t) = T_0 + (T_{max}\text{-}T_0)e^{-Bt}$. According to the definition of the energy absorption-related parameter A in equation (1), the photothermal efficiency η can be calculated by

$$\eta = \frac{AmC}{P\left(1 - 10^{-A_\lambda}\right)} \tag{3}$$

By fitting the experimental cooling curve with the temperature function $T_c(t)$, the parameter B related to the energy dissipation can be obtained. Substituting the value of B into the temperature function $T_h(t)$ and fitting it to the experimental heating curve yield the value of parameter A, which is used to determine the photothermal efficiency η.

Optical microscopy. Bright field microscopic images of LCE composite films were obtained using an optical microscope (Leica, CTR5000). Particle size analysis was done with imageJ, where aggregates were defined as particles of diameter larger than 2 μm.

Fourier transformation infrared (FTIR) spectroscopy. Fourier transformation infrared spectra of CS and CNT were measured using an FTIR spectrometer (Agilent technologies, Cary 660 FTIR) with KBr pellet method. To make the KBr pellets for FTIR measurements, 6 mg of CS or CNT was grinded together with 294 mg of KBr and mixed thoroughly with a vortex mixer. 30 mg of the mixed powder was then grinded together again with 270 mg of KBr and mixed thoroughly with a vortex mixer to produce 300 mg of KBr containing 0.02% weight of CS or CNT, which was pressed using a hydraulic presser to form a KBr pellet. The KBr pellets were dried at 60°C for 48 h before measurements to remove the moisture.

Dynamic mechanical analysis (DMA) and actuation strain/stress characterization. Dynamic mechanical analysis and

actuation strain/stress characterizations were performed using with a dynamic mechanical analyzer (TA instruments, DMA850). For all measurements, LCE-CS and LCE-CNT composites were cut into rectangular shape of 25 × 7 × 0.16 mm in dimensions and tested in tensile mode. All samples were annealed at 150°C for 1 min and cooled to room temperature. Measurements were done after letting the samples stand for 5 min at room temperature. For DMA, the samples were cycled with 20 μm stretch (corresponding to 0.1% strain after subtracting the length that is clamped) at 1 Hz and heated from 30 to 145°C at a heating rate of 3°C/min. The T_{NI} of the samples were characterized by an abrupt decrease in storage modulus. For actuation strain measurements, the samples were kept taut at a constant small stress of 0.01 Mpa. The samples were heated from 30 to 145°C at a heating rate of 5°C/min and the strain was recorded. For actuation stress measurements, the samples were held at a constant strain of 0.2%. The samples were heated from 30 to 100°C at a heating rate of 5°C/min and the stress was recorded. The stress strain curves of samples were measured after equilibrating the samples at 25, 60, 100, or 140°C for 1 min. The samples were stretched at a strain rate of 15%/min.

Actuation of photo-oscillator and characterization of deformation and motion

Self-oscillation of photo-oscillator. Strip-shaped photo-oscillators were fixed on one end and hung vertically in the relaxed state. The photo-oscillators were actuated using either an 808 nm NIR spot laser (Q-Baihe, LSR808NL), a 635 nm red laser (Q-Baihe, LSR635NL-100) or a 532 nm green laser (Coherent, Genesis MX532-1000 STM), that irradiate on a specific position on the sample. The motion was recorded using a camera (Canon, EOS70D).

Results and discussion

Materials characterization

Optical properties and photothermal conversion efficiency of photothermal agents and LCE-CS composite. To investigate the optical properties of LCE composites, we dispersed CS and CNT (as control) in both ethylene glycol and LCE matrix and measured the absorption spectra in the UV-Vis-NIR range. The UV-Vis-NIR spectra were compared with CNT. As shown in Figure 2(a) (top), at a low concentration of 20 μg/mL in ethylene glycol, both CS and CNT have high absorbance, which increases from the NIR region (~800 nm) to UV region (~300 nm). Throughout the wavelength range, CS exhibits higher absorbance than CNT, which indicates higher photothermal conversion efficiency. Similarly, the UV-Vis-NIR spectra of LCE-CS and LCE-CNT composites of 0.5 wt% (LCE-0.5CS and LCE-0.5CNT, number indicating weight percentage of photothermal agents) suggest that CS is more absorptive in wavelengths higher than 325 nm (Figure 2(a), bottom). We theorized that the high absorbance of CS can be partially attributed to its better dispersion in polar solvents, including ethylene glycol and LCE. This observation was consistent with existing literature supporting the great dispersibility of CS in polar solvents.[45] According to the FTIR spectra of KBr pellets of CS and CNT shown in Figure 2(b), both samples have absorption peaks at 2800-3000 cm^{-1}, which are assigned to aliphatic saturated C-H.[46,47] The strong absorption peak of CS at 3438 cm^{-1} corresponds to O-H bond stretching, and the peak at 1731 cm^{-1} corresponds to C = O stretching, while these peaks are extremely weak in CNT.[46] Both functional groups might form polar interactions with solvents and host polymers, facilitating the dispersion of CS in LCE matrix that contains polar functional groups including ester and sulfide linkages. This hypothesis is consistent with existent literature suggesting oxygenated surface functionalization of CNT including carboxyl group, carbonyl groups, ether, and unbound hydroxyl groups of phenol is crucial for its dispersion and solubility.[47] Meanwhile, for the CNT FTIR spectrum, the weak absorption peak of O-H and C = O indicate the low concentration of these bonds. The signal at 1624 cm^{-1} is assigned to the C = C bonds.[47] The absorption peaks at 1263 and 1384 cm^{-1} suggest that CNT used in this study might be functionalized with nitrogen doping, which are attributed to N-CNT, and N-N bonds, respectively.[47] Despite the possible N heteroatoms, the lack of amine groups (indicated by weak signal of N-H in the ~3400 cm^{-1} region) render it unfavorable for polar interaction with the polymer matrix, while strong Van der Waals interaction can cause agglomeration of CNT.[47,48] Due to the better dispersion of CS in polar solvents or host polymers, the effective area exposed to the light is larger compared to a heavily aggregated solution of CNT. To confirm the hypothesis, optical microscopic image of LCE-0.5CS (Figure 2(c), top left) shows significantly fewer aggregates with smaller sizes (average aggregate diameter of 6.1 μm) than LCE-0.5CNT (Figure 2(c), middle left) (average aggregate diameter of 15.8 μm) (see experimental), further supporting the uniform dispersion of CS in the LCE matrix. In addition, we find that the aggregate size of CS increases slightly to 6.9 μm in LCE-1.0CS (Figure 2(c), bottom left) compared to LCE-0.5CS, suggesting an optimal concentration exists for uniform distribution. The distribution of aggregate sizes is shown in Figure 2(c).

Next, we examined the photothermal conversion performance of the LCE-CS and LCE-CNT composites. We monitored the time-dependent temperature change of the samples surfaces with 808 nm laser irradiation at different light intensities. Upon irradiation (t = 0 s), the temperature increases and reaches a plateau within less than 10 s, where

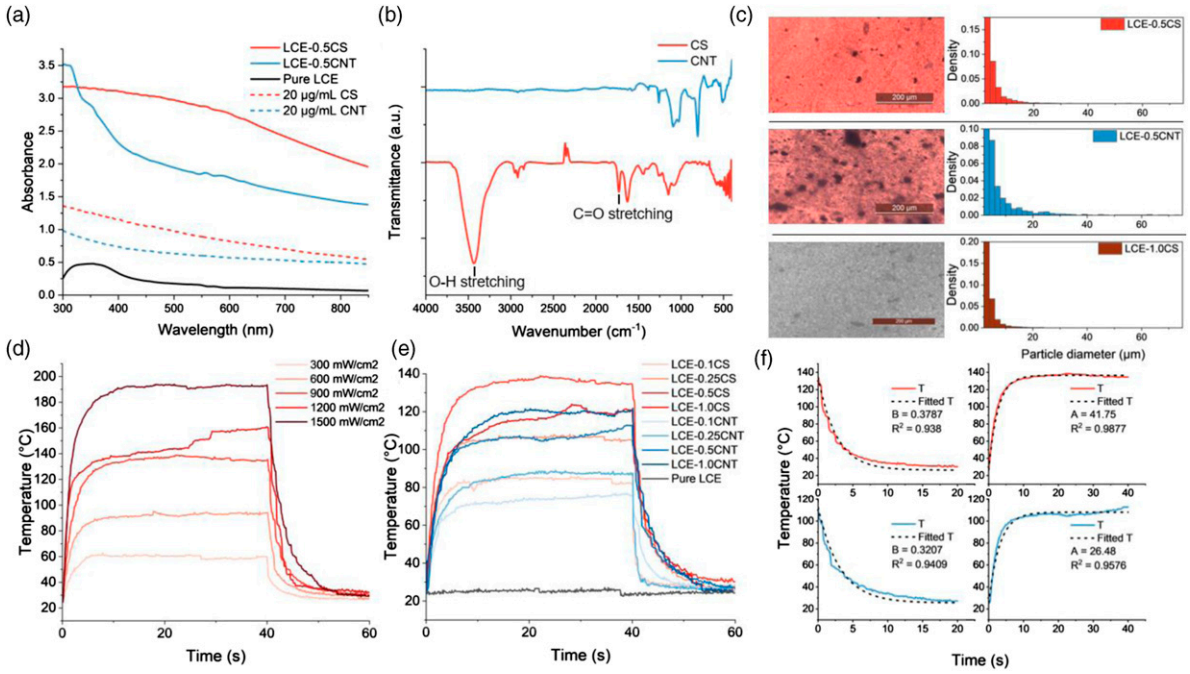

Figure 2. Optical properties and photothermal conversion efficiencies of LCEs-CS and LCE-CNT composites. (a) Absorption spectra of CS and CNT dispersed in ethylene glycol (dashed lines) and pure LCE, LCE-0.5CS, and LCE-0.5CNT (solid lines). (b) FTIR spectra of CS and CNT. (c) Bright field microscopic images of LCE-0.5CS (top left), LCE-0.5CNT (middle left) and LCE-1.0CS (bottom left), and corresponding particle diameter distribution (top right, middle right, and bottom right). Scale bar is 200 μm (d) Photothermal conversion efficiency characterized by the temperature rise of LCE-0.5CS under 808 nm laser with light intensities of 300, 600, 900, 1200, and 1500 mW/cm^{-2}. (e) Photothermal conversion efficiency characterized by the temperature rise of pure LCE, LCE-0.1CS, LCE-0.25CS, LCE-0.5CS, LCE-1.0CS, LCE-0.1 CNT, LCE-0.25CNT, LCE-0.5CNT, and LCE-1.0CNT under 808 nm laser of 900 mW/cm^{-2}. (f) Temperature variation versus time and fitted temperature of LCE-0.5CS (top left: cooling; top right: heating) and LCE-0.5CNT (bottom left: cooling; bottom right: heating) at 900 mW/cm^2.

a dynamic thermal equilibrium is achieved between photothermal effect and heat dissipation to the ambient atmosphere. A higher power input of light leads to more rapid rise of temperature and a higher equilibrium temperature for the same sample (Figure 2(d)). Under 900 mW/cm^2, LCE-0.5CS reaches a higher equilibrium temperature (120°C) compared to LCE-0.5CNT (105°C), further indicating the higher photothermal conversion efficiency of LCE-CS than that of LCE-CNT composites, which agrees with our UV-Vis-NIR spectra measurements (Figure 2(a)). When irradiation was turned off (t = 40 s), the temperature of samples dropped rapidly to room temperature, proving their good thermal conduction. To find out the optimal concentration of photothermal agent, we varied CS concentrations from 0.1 to 1.0 wt % dispersed in LCE and measured temperature elevation profile (Figure 2(e)). Pure LCE exhibits temperature elevation of <3°C at 900 mW/cm^2, indicating its minimal photothermal effect. In contrast, best photothermal conversion performance was achieved with 0.5 wt% addition of CS, demonstrating an equilibrium temperature as high as 137°C, which is 25°C higher than LCE-0.5CNT sample and 16°C higher than LCE-1.0CS sample. As indicated above, the higher equilibrium temperature of LCE-0.5CS might be attributed to the better dispersion of photothermal agent and smaller aggregate sizes. To calculate the photothermal efficiency of these composites, the temperature variation of LCE-0.5CS and LCE-0.5CNT was fitted as described in the experimental section. The fitting results of the cooling curves are shown in Figure 2(f) (top left, bottom left). For the LCE-0.5CS, B = 0.3787 and the coefficient of determination R^2 = 0.938. For the LCE-0.5CNT, B = 0.3207 and R^2 = 0.9409. After calculating the value of B, the fitting results of the heating curves have been summarized in Figure 2(f) (top right, bottom right). For LCE-0.5CS, A = 41.75 and R^2 = 0.9877. For LCE-0.5CNT, A = 26.48 and R^2 = 0.9576. Finally, by substituting the value of A and other material properties, the photothermal conversion efficiency η can be calculated based on equation (3). For LCE-0.5CS, η = 45.7%, while for LCE-0.5CNT, η = 29.0%, which further demonstrates that candle soot can effectively improve the photothermal conversion efficiency of LCE.

Characterization of mechanical and thermomechanical properties. We have studied the mechanical properties by a DMA system. The dynamic moduli of LCE-0.5CS are compared with LCE-0.5CNT and pure LCE (Figure 3(a)).

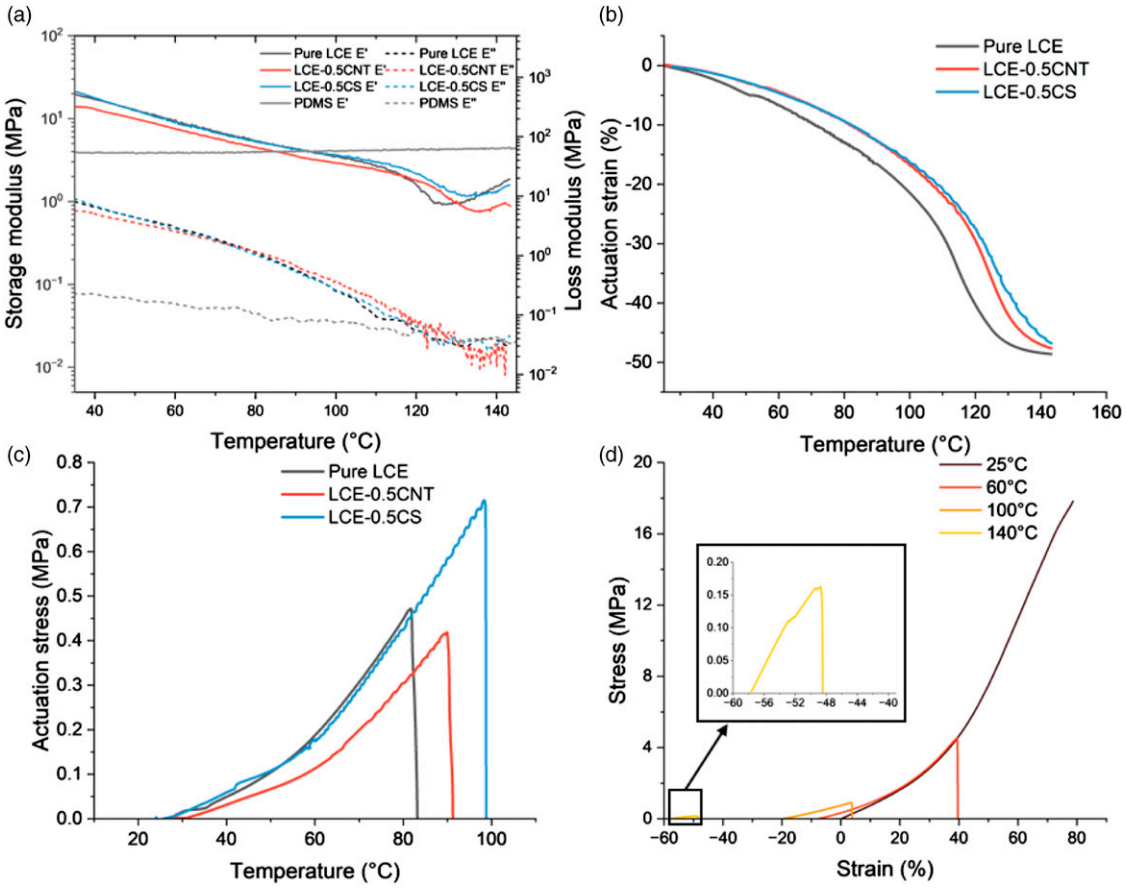

Figure 3. Mechanical properties of LCE composites characterized by dynamic mechanical analysis (DMAs). (a) Storage moduli (E') and loss moduli (E'') of LCE, LCE-0.5CS, LCE-0.5CNT and PDMS. (b) actuation strain, and (c) actuation stress of pure LCE, LCE-0.5CS and LCE-0.5CNT. (d) Stress-strain curves of LCE-0.5CS at 25, 60, 100, and 140°C, where strain was calculated with respect to original length of the sample at room temperature. Inset is the zoomed stress-strain curve at 140°C.

For all samples, the storage moduli decrease with rising temperature from about 20 MPa at room temperature, until T_{NI} is reached, as signified by a local minimum of the storage modulus, and increases again above T_{NI}. Such a profile of storage moduli is typical for thiol-acrylate LCE.[34] The T_{NI} values of LCE-0.5CS (131°C) and LCE-0.5CNT (134°C) are slightly higher than pure LCE (126°C). Meanwhile, all samples show similar magnitude of storage moduli, suggesting negligible stiffening effect of carbon-based fillers.

Actuation strain $\varepsilon(T)$ is calculated using the formula $\varepsilon(T) = \frac{L-L_0}{L_0}$, where L is the instant length of the LCE film at temperature T, and L_0 is the length at room temperature. According to Figure 3(b), although pure LCE exhibits slightly larger actuation strain at all temperatures over the tested range, all three samples reach remarkable actuation strain of about −45% strain at 140°C. Furthermore, LCE-0.5CS and LCE-0.5CNT have almost identical actuation strain up to 100°C. As a result, the photothermal agents minimally affect the actuation strain of LCE. In addition, the produced actuation stress of LCE-CS at given temperature showed similar performance compared to that of pure LCE, and is higher than that of LCE-CNT (Figure 3(c)). At higher temperatures, the LCE films fracture due to large thermal stress. Among the three samples, LCE-0.5CS fails at the temperature of 98°C, achieving a failure stress of 0.71 MPa, both higher than other samples, implying that LCE-0.5CS is most suitable for high-temperature working conditions. The better thermomechanical properties of LCE-0.5CS might be caused by the carboxylic groups in CS binding to polymer chains at an appropriate concentration, as supported by Figure 2(b).[49] In contrast, the lower storage modulus (Figure 3(a)) and failure stress of LCE-0.5CNT (Figure 3(c)) might be attributed to the agglomerates of CNT in the LCE matrix (Figure 2(c), bottom left), which can function as defects where cracks are initiated, rendering it more susceptible to failure under thermal stress.[49] In addition, we show the stress-strain curves of LCE-0.5CS at 25, 60, 100, and 140°C as an example to further analyze the thermomechanical properties of the LCE composites

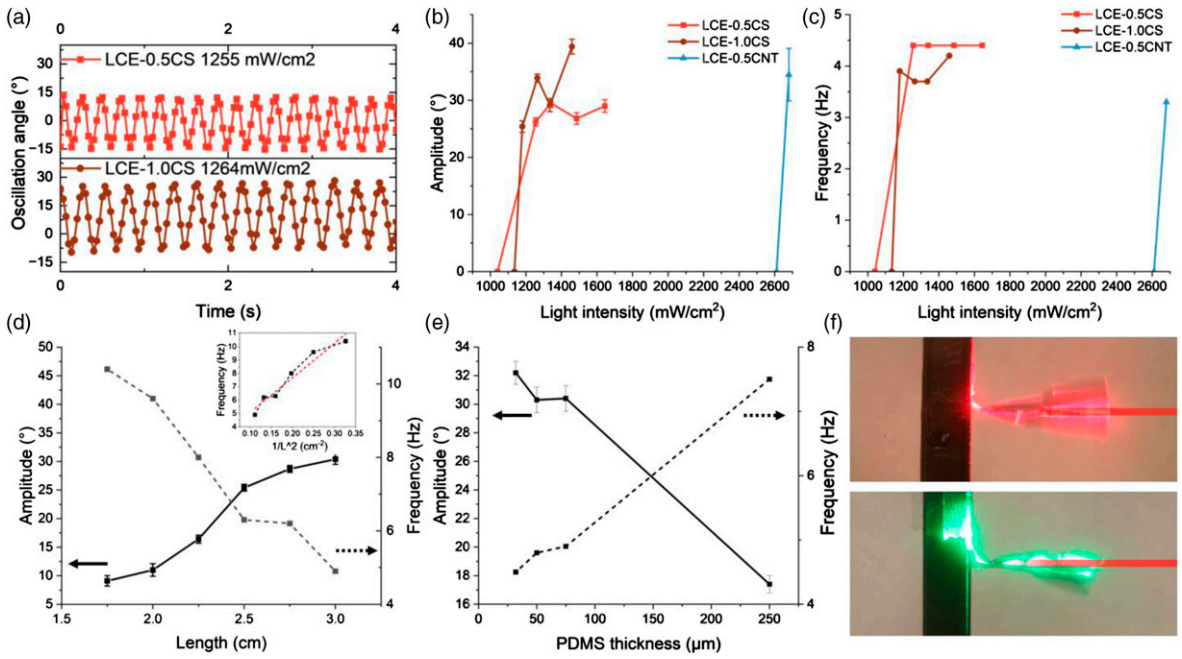

Figure 4. Oscillation behavior of the oscillator (a) Oscillation angle of LCE-0.5CS/PDMS (top) and LCE-1.0CS/PDMS (bottom) (length is 3 cm, LCE thickness is 160 μm, PDMS thickness is 75 μm) varies with time under 808 nm laser at 1255 and 1264 mW/cm^2, respectively. (b) Oscillation amplitude and (c) frequency of oscillators (length is 3 cm, LCE thickness is 160 μm, PDMS thickness is 75 μm) under 808 nm laser at different light intensities. (d) Oscillation behavior of LCE-0.5CS/PDMS with varying lengths under 808 nm laser of 1360 mW/cm^{-2} (LCE thickness is 160 μm, PDMS thickness is 75 μm). Inset: oscillation frequency plotted against inverse square of length. Red dashed line represents linear fit of frequency vs inverse square of length, $R^2 = 0.94$. (e) Oscillation behavior of LCE-0.5CS/PDMS with varying PDMS thicknesses under 808 nm laser of 1360 mW/cm^2 (length is fixed at 3 cm). (f) Oscillation of LCE-0.5CS/PDMS under 635 nm irradiation (top) and 532 nm irradiation (bottom). Red beams show light direction.

(Figure 3(d)). As the temperature increases, the Young's modulus extracted from the stress-strain curves decreases significantly (9.3, 4.3, 2.6, 1.5 MPa at 25, 60, 100, 140°C, respectively), which is consistent with the storage moduli results in Figure 3(a). Also, the starting strains of the tensile tests (at which stress is zero) agree with the actuation strain in Figure 3(b). These trends are due to the softening of the polymer matrix and loss of mesogen alignment at high temperatures, which lead to decrease of the failure stress of the LCE composite. With the outperformed photothermal, mechanical, and thermomechanical performance, we chose LCE-0.5CS for all future characterizations and fabrications and contrasted it with LCE-1.0CS and LCE-0.5CNT for comparison.

Self-oscillation of photo-oscillator. The oscillation behavior of LCE-0.5CS/PDMS has been investigated and compared with LCE-0.5CNT/PDMS and LCE-1.0CS/PDMS. The monodomain LCE composites are 160 μm thick after UV cross-linking at stretched state, and adhered to PDMS films with well-defined thickness of 75 μm (See experimental). The oscillator is placed vertically as the initial state and the NIR laser is applied horizontally to the LCE side. The oscillation angle over time of an LCE-0.5CS/PDMS sample and an LCE-1.0CS/PDMS sample of the same length (3 cm) under 808 nm irradiation of similar intensities (1255 and 1264 mW/cm^2, respectively) is plotted in Figure 4(a). The oscillation amplitude is defined as the tip-to-tip angular displacement in this work, and oscillation frequency can be extracted by performing a Fourier transformation of the oscillation angle. The amplitude and frequency of LCE-0.5CS/PDMS, LCE-0.5CNT/PDMS, and LCE-1.0CS/PDMS are shown in Figure 4(b) and (c). At low light intensities, the irradiation cannot heat the hinge to sufficiently high temperature to initiate bending of the bilayer past the equilibrium position. As a result, tracking behavior instead of self-oscillation is observed. When light intensity is higher than a threshold, the angular momentum of LCE bending is large enough to move the bilayer out of mechanical equilibrium, thus initiating the self-shadowing process described before and self-oscillation is achieved. Oscillation amplitude follows a staggered trend with a higher light intensity, which is not completely concordant with the second-order transition behavior of LCE as previously reported, where amplitude should increase in proportional to $(I - I_{threshold})^{1/2}$.[32] On the other hand, the frequency remains relatively unchanged when light intensity increases since the natural frequency of these photo-oscillators does not change much due to their stable mechanical properties and dimensions.

When the light intensity is further increased, the hinges of the oscillators are overheated and can no longer relax and cool below the equilibrium temperature. Consequently, the negative feedback loop of temperature required for self-oscillation is broken, and the oscillators will stay static at a large bending angle ("overshooting"). According to Figure 4(b) and (c), although all oscillators achieve similar oscillation amplitudes and frequencies, LCE-CS/PDMS samples have much lower intensity thresholds and wider operation windows than LCE-CNT/PDMS. By contrast, the LCE-CNT/PDMS overshoots when the intensity is only 150 mW/cm^2 higher than the threshold.

The oscillation behavior of these oscillators is also tunable by adjusting their lengths and thicknesses of PDMS films used to form the bilayer (Figure 4(d) and (e)). As the length of the oscillator is lowered, the amplitude will also decrease while the frequency will increase at a given light intensity. According to the formula of natural frequency of a cantilever beam $f_n = \frac{K_n}{2\pi}\sqrt{\frac{EIg}{wL^4}}$, where E is the elastic modulus, I is the area moment of inertia, w is the load per unit length, and L is the length of the beam, the frequency should vary linearly with the inverse square of the length of the beam.[50] According to the inset of Figure 4(d), the relationship fits well for the oscillation frequency. Meanwhile, a higher PDMS thickness will also increase the frequency and decrease the amplitude. This can be explained by the increased area moment of inertia leading to higher natural frequency. It is noteworthy that our oscillators can successfully achieve oscillation frequencies, comparable to literature values for LCN oscillators with storage moduli that are 1-3 orders of magnitude higher than LCE. This is partially attributed to the low viscoelasticity of PDMS ($\tan\delta = 0.07$, calculated from data in Figure 2(a) at 30°C) that reduces the damping of the system and facilitates the rapid the actuation-recovery cycle. As a result, the less favorable slow heat dissipation to ambient environment and a delayed LCE recovery after cooling are overcome to some extent.[51,52]

We have also demonstrated that the composite can be actuated by light of a wide spectrum of wavelengths. As indicated previously in Figure 2(a), CS effectively absorbs light in the visible and NIR range. Motivated by this property, we used a 635 nm laser and a 532 nm laser to successfully achieve self-oscillation of the bilayer (Figure 4(f)), suggesting a low wavelength requirement for the light source. This may open up possibilities for application under broad scenarios, including actuation under concentrated sunlight.

Conclusions

In this work, we developed a design and a fabrication method to create light-powered self-oscillators made of LCE-CS/PDMS bilayer via thiol-acrylate Michael addition polymerization. Photothermal oscillation is achieved with self-shadowing mechanism enabled by CS as a superior photothermal agent with excellent compatibility with LCE matrix. The self-oscillation behavior can be tuned by adjusting the light intensity, as well as the length and the PDMS thickness of the bilayer. Lastly, we have demonstrated that the oscillator can be actuated with a wide spectrum of irradiation, indicating applicability to different light conditions.

Declaration of conflicting interests

The authors declared no potential conflicts of interest with respect to the research, authorship, and/or publication of this article.

Funding

The author(s) disclosed receipt of the following financial support for the research, authorship, and/or publication of this article: This work is supported by AFOSR awards FA9550-17-1-0311, FA9550-18-1-0449 and FA9550-20-1-0344, and ONR awards N000141712117 and N00014-18-1-2314.

ORCID iD

Ximin He https://orcid.org/0000-0001-8845-4637

References

1. Lancia F, Ryabchun A and Katsonis N. Life-like motion driven by artificial molecular machines. *Nat Rev Chem* 2019; 3: 536–551. DOI: 10.1038/s41570-019-0122-2.
2. McCracken JM, Donovan BR and White TJ. Materials as machines. *Adv Mater* 2020; 32: 1906564. DOI: 10.1002/adma.201906564. ARTN 1906564.
3. Yu L, Si PX, Bauman L, et al. Synergetic combination of interfacial engineering and shape-changing modulation for biomimetic soft robotic devices. *Langmuir* 2020; 36: 3279–3291. DOI: 10.1021/acs.langmuir.9b03773.
4. Li CS, Liu Y, Huang XZ, et al. Direct sun-driven artificial heliotropism for solar energy harvesting based on a photo-thermomechanical liquid-crystal elastomer nanocomposite. *Adv Funct Mater* 2012; 22: 5166–5174. DOI: 10.1002/adfm.201202038.
5. Zhang J, Guo Y, Hu W, et al. Liquid crystal elastomer-based magnetic composite films for reconfigurable shape-morphing soft miniature machines. *Adv Mater* 2021; 33: e2006191. DOI: 10.1002/adma.202006191.
6. Greco F, Domenici V, Romiti S, et al. Reversible heat-induced microwrinkling of PEDOT:PSS nanofilm surface over a monodomain liquid crystal elastomer. *Mol Crystals Liquid Crystals* 2013; 572: 40–49. DOI: 10.1080/15421406.2012.763208.

7. Chen T, Bilal OR, Shea K, et al. Harnessing bistability for directional propulsion of soft, untethered robots. *Proc Natl Acad Sci* 2018; 115: 5698–5702.
8. Yang ZH, Wang QH and Wang TM. Dual-triggered and thermally reconfigurable shape memory graphene-vitrimer composites. *Acs Appl Mater Inter* 2016; 8: 21691–21699. DOI: 10.1021/acsami.6b07403.
9. Li G, Wang SW, Liu ZT, et al. 2D-to-3D shape transformation of room-temperature-programmable shape-memory polymers through selective suppression of strain relaxation. *Acs Appl Mater Inter* 2018; 10: 40189–40197. DOI: 10.1021/acsami.8b16094.
10. Zhao Y, Xuan C, Qian X, et al. Soft phototactic swimmer based on self-sustained hydrogel oscillator. *Sci Robotics* 2019; 4: eaax7112. DOI: 10.1126/scirobotics.aax7112
11. Kim YS, Liu M, Ishida Y, et al. Thermoresponsive actuation enabled by permittivity switching in an electrostatically anisotropic hydrogel. *Nat Mater* 2015; 14: 1002–1007. DOI: 10.1038/nmat4363.
12. Zhou Y, Hauser AW, Bende NP, et al. Waveguiding microactuators based on a photothermally responsive nanocomposite hydrogel. *Adv Funct Mater* 2016; 26: 5447–5452. DOI: 10.1002/adfm.201601569.
13. Ahn C, Li K and Cai S. Light or thermally powered autonomous rolling of an elastomer rod. *ACS Appl Mater Inter* 2018; 10: 25689–25696. DOI: 10.1021/acsami.8b07563.
14. Chen Z, Liu J, Chen YJ, et al. Multiple-stimuli-responsive and cellulose conductive ionic hydrogel for smart wearable devices and thermal actuators. *Acs Appl Mater Inter* 2021; 13: 1353–1366. DOI: 10.1021/acsami.0c16719.
15. Zhou SZ, Wu BY, Zhou Q, et al. Ionic strength and thermal dual-responsive bilayer hollow spherical hydrogel actuator. *Macromol Rapid Comm* 2020; 41: 1900543. DOI: 10.1002/marc.201900543. ARTN 1900543.
16. van Oosten CL, Bastiaansen CW and Broer DJ. Printed artificial cilia from liquid-crystal network actuators modularly driven by light. *Nat Mater* 2009; 8: 677–682. DOI: 10.1038/nmat2487.
17. Gelebart AH, Jan Mulder D, Varga M, et al. Making waves in a photoactive polymer film. *Nature* 2017; 546: 632–636. DOI: 10.1038/nature22987.
18. Kumar K, Knie C, Bleger D, et al. A chaotic self-oscillating sunlight-driven polymer actuator. *Nat Commun* 2016; 7: 11975. DOI: 10.1038/ncomms11975.
19. Feng W, Broer DJ and Liu D. Combined light and electric response of topographic liquid crystal network surfaces. *Adv Funct Mater* 2020; 30: 1901681. DOI: 10.1002/adfm.201901681.
20. Pelrine R, Kornbluh R, Pei Q, et al. High-speed electrically actuated elastomers with strain greater than 100%. *Science* 2000; 287: 836–839. DOI: 10.1126/science.287.5454.836.
21. Kim Y, Yuk H, Zhao R, et al. Printing ferromagnetic domains for untethered fast-transforming soft materials. *Nature* 2018; 558: 274–279. DOI: 10.1038/s41586-018-0185-0.
22. Park JE, Jeon J, Cho JH, et al. Magnetomotility of untethered helical soft robots. *RSC Adv* 2019; 9: 11272–11280. DOI: 10.1039/C9RA01775E.
23. Jiang Y, Korpas LM and Raney JR. Bifurcation-based embodied logic and autonomous actuation. *Nat Commun* 2019; 10: 128. DOI: 10.1038/s41467-018-08055-3.
24. Zhu H, Xu BR, Wang Y, et al. Self-powered locomotion of a hydrogel water strider. *Sci Robotics* 2021; 6: eabe7925. DOI: 10.1126/scirobotics.abe7925. ARTN eabe7925.
25. Zeng H, Wasylczyk P, Wiersma DS, et al. Light robots: bridging the gap between microrobotics and photomechanics in soft materials. *Adv Mater* 2018; 30: 1703554, DOI: 10.1002/adma.201703554. ARTN 1703554.
26. Hu Y, Li Z, Lan T, et al. Photoactuators for direct optical-to-mechanical energy conversion: from nanocomponent assembly to macroscopic deformation. *Adv Mater* 2016; 28: 10548–10556. DOI: 10.1002/adma.201602685.
27. Hu J, Wang W and Yu H. Endowing soft photo-actuators with intelligence. *Adv Intell Syst* 2019; 1. 1900050, DOI: 10.1002/aisy.201900050.
28. White TJ and Broer DJ. Programmable and adaptive mechanics with liquid crystal polymer networks and elastomers. *Nat Mater* 2015; 14: 1087–1098. DOI: 10.1038/nmat4433.
29. Mehta K, Peeketi AR, Liu L, et al. Design and applications of light responsive liquid crystal polymer thin films. *Appl Phys Rev* 2020; 7: 041306. DOI: 10.1063/5.0014619.
30. Dong L and Zhao Y. Photothermally driven liquid crystal polymer actuators. *Mater Chem Front* 2018; 2: 1932–1943. DOI: 10.1039/c8qm00363g.
31. Herbert KM, Fowler HE, McCracken JM, et al. Synthesis and alignment of liquid crystalline elastomers. *Nat Rev Mater* 2021; 7: 23–38, DOI: 10.1038/s41578-021-00359-z.
32. Serak S, Tabiryan N, Vergara R, et al. Liquid crystalline polymer cantilever oscillators fueled by light. *Soft Matter* 2010; 6: 779–783. DOI: 10.1039/b916831a.
33. Gelebart AH, Vantomme G, Meijer EW, et al. Mastering the photothermal effect in liquid crystal networks: a general approach for self-sustained mechanical oscillators. *Adv Mater* 2017; 29: 1606712, DOI: 10.1002/adma.201606712.
34. Saed MO, Torbati AH, Starr CA, et al. Thiol-acrylate main-chain liquid-crystalline elastomers with tunable thermomechanical properties and actuation strain. *J Polym Sci B Polym Phys* 2017; 55: 157–168. DOI: 10.1002/polb.24249.
35. Lu XL, Zhang H, Fei GX, et al. Liquid-Crystalline dynamic networks doped with gold nanorods showing enhanced photocontrol of actuation. *Adv Mater* 2018; 30: 1706597. DOI: 10.1002/adma.201706597. ARTN 1706597.
36. Ahn C, Liang X and Cai S. Bioinspired design of light-powered crawling, squeezing, and jumping untethered soft robot. *Adv Mater Tech* 2019; 4; 1900185. DOI: 10.1002/admt.201900185.
37. Shen C, Lan R, Huang R, et al. Photochemically and photothermally controllable liquid crystalline network and soft

walkers. *ACS Appl Mater Inter* 2021; 13: 3221–3227. DOI: 10.1021/acsami.0c20628.
38. Wu S, Du Y, Alsaid Y, et al. Superhydrophobic photothermal icephobic surfaces based on candle soot. *Proc Natl Acad Sci* 2020; 117: 11240–11246. DOI: 10.1073/pnas.2001972117.
39. Zhang L, Bai B, Hu N, et al. Low-cost and facile fabrication of a candle soot/adsorbent cotton 3D-interfacial solar steam generation for effective water evaporation. *Solar Energ Mater Solar Cell* 2021; 221: 110876. DOI: 10.1016/j.solmat.2020.110876.
40. Mulay MR, Chauhan A, Patel S, et al. Candle soot: journey from a pollutant to a functional material. *Carbon* 2019; 144: 684–712. DOI: 10.1016/j.carbon.2018.12.083.
41. Qahtan TF, Gondal MA, Alade IO, et al. Fabrication of water jet resistant and thermally stable superhydrophobic surfaces by spray coating of candle soot dispersion. *Sci Rep* 2017; 7: 7531. DOI: 10.1038/s41598-017-06753-4.
42. Sutar RS, Latthe SS, Sargar AM, et al. Spray deposition of PDMS/candle soot NPs composite for self-cleaning superhydrophobic coating. *Macromolecular Symposia* 2020; 393: 2000031. DOI: 10.1002/masy.202000031.
43. Breitenborn H, Dong J, Piccoli R, et al. Quantifying the photothermal conversion efficiency of plasmonic nanoparticles by means of terahertz radiation. *Apl Photon* 2019; 4: 126106. DOI: 10.1063/1.5128524. Artn 126106.
44. Torras N, Zinoviev KE, Esteve J, et al. Liquid-crystalline elastomer micropillar array for haptic actuation. *J Mater Chem C* 2013; 1: 5183–5190. DOI: 10.1039/c3tc31109k.
45. Zhang R, Liu Y-B and Sun S-Q. Preparation of highly luminescent and biocompatible carbon dots using a new extraction method. *J Nanoparticle Res* 2013; 15: 2010. DOI: 10.1007/s11051-013-2010-x.
46. Sahoo BN and Kandasubramanian B. An experimental design for the investigation of water repellent property of candle soot particles. *Mater Chem Phys* 2014; 148: 134–142. DOI: 10.1016/j.matchemphys.2014.07.022.
47. Tucureanu V, Matei A and Avram AM. FTIR spectroscopy for carbon family study. *Crit Rev Anal Chem* 2016; 46: 502–520. DOI: 10.1080/10408347.2016.1157013.
48. Konya Z, Vesselenyi I, Niesz K, et al. Large scale production of short functionalized carbon nanotubes. *Chem Phys Lett* 2002; 360: 429–435. DOI: 10.1016/S0009-2614(02)00900-4.
49. Salah N, Alfawzan AM, Saeed A, et al. Effective reinforcements for thermoplastics based on carbon nanotubes of oil fly ash. *Sci Rep-uk* 2019; 9. 20288, DOI: 10.1038/s41598-019-56777-1. ARTN 20288.
50. Roark RJ, Budynas RG and Sadegh AM. *Roark's formulas for stress and strain*. 9th ed. New York: McGraw-Hill Education, 2020, p. 1. Online: resource (xvi, 907 pages).
51. Huang XN, Michael F, Patterson ZJ, et al. Shape memory materials for electrically-powered soft machines. *J Mater Chem B* 2020; 8: 4539–4551. DOI: 10.1039/d0tb00392a.
52. Liu HR, Tian HM, Shao JY, et al. An electrically actuated soft artificial muscle based on a high-performance flexible electrothermal film and liquid-crystal elastomer. *Acs Appl Mater Inter* 2020; 12: 56338–56349. DOI: 10.1021/acsami.0c17327.